catalysts

MDPI

Article

Metal-Free Cellulose Carbon Nanofiber Supported Graphitic Carbon Nitride for High-Efficient BPA Degradation by Photcatalytic Peroxymonosulfate Activation

Jingjing Liu, Guilong Gao and Lu Gan *

College of Materials Science and Engineering, Nanjing Forestry University, Nanjing 210037, China; liujingjing200503@163.com (J.L.); gaoguilong@njfu.edu.cn (G.G.)
* Correspondence: ganlu@njfu.edu.cn

Abstract

Herein, carbon nanofiber (CNF) was prepared by pyrolyzing electrospun cellulose nanofiber, which was further used to incorporate with graphitic carbon nitride (g-C_3N_4) to prepare metal-free photocatalyst (CNF/g-C_3N_4). CNF/g-C_3N_4 was then used to degrade bisphenol A (BPA) under visible light with the assistance of peroxymonosulfate (PMS). It was illustrated from the results that CNF with conjugated aromatic structure could significantly enhance the light absorption range and capability. At the existence of PMS, 0.5 g/L of CNF/g-C_3N_4 could efficiently degrade 0.05 mM of BPA within 45 min with a high total organic carbon removal rate of >70% under visible light. It was found that the reaction system could generate various reactive oxygen species (ROSs) including hydroxyl radical, superoxide radical and singlet oxygen for BPA degradation. Due to the existence of these species, the reaction system exhibited high performance adaptability towards abundant water matrices and high stability under consecutive runs. This work prospects a new strategy to develop a high-performance advanced oxidation system for quick organic pollutant degradation and mineralization.

Keywords: cellulose; carbon nanofiber; graphitic carbon nitride; composite photocatalyst; peroxymonosulfate; organic pollutant degradation

Academic Editors: Edward G. Gillan and Jorge Bedia

Received: 30 June 2025
Revised: 8 August 2025
Accepted: 14 August 2025
Published: 18 August 2025

Citation: Liu, J.; Gao, G.; Gan, L. Metal-Free Cellulose Carbon Nanofiber Supported Graphitic Carbon Nitride for High-Efficient BPA Degradation by Photcatalytic Peroxymonosulfate Activation. *Catalysts* **2025**, *15*, 788. https://doi.org/10.3390/catal15080788

1. Introduction

Water contamination caused by excessive discharge of refractory organic pollutants (ROPs) such as drugs and personal care products, endocrine disruptors, and pesticides has been regarded as a serious threat to the ecosystem of humans recently [1]. ROPs generally are hard to remove by traditional sewage treatment means due to their stable structures [2]. Moreover, trace concentration of ROPs can cause severe damage to the human body, since most of these ROPs are highly toxic, which can easily accumulate in human organs and cause serious diseases [3]. Bisphenol A (BPA) as a typical endocrine-disrupting ROP has received tremendous attention since it has been frequently detected in various water bodies all over the world. More seriously, the concentrations of the detected BPA were much higher than that of the regulated standards in many countries [4]. Numerous studies have illustrated that BPA can affect the growth, development and reproduction of humans by destroying sex hormones. Advanced oxidation processes (AOPs) have received tremendous research interest in the area of prompt ROP removals since most AOPs can generate a variety of highly reactive oxygenated species (ROSs), including radicals and

non-radicals, which are able to quickly attack ROPs in water with a high mineralization rate [5]. Amongst all AOPs, semiconductor-based photocatalysis is a feasible solution for solving ROP pollution in water by harvesting solar energy to initiate electron–hole pair separations and subsequently produce abundant ROSs [6]. Graphitic carbon nitride (g-C_3N_4), a metal-free photocatalyst with a proper band gap energy of 2.70 eV, has shown enormous potential in ROP degradation since it can absorb visible light as energy and does not bring about secondary pollution to the water matrix during the whole process [7]. However, its practical applications have been significantly restricted due to the nature of slow charge mobility and fast recombination of photogenerated electron–hole pairs, which result in a low quantum utilization rate under light irradiations [8].

Many strategies have been proposed to overcome the defects. One of the applicable approaches is to incorporate carbonaceous materials with g-C_3N_4 [9]. Carbonaceous materials usually have a large specific area, which can promote the dispersion of g-C_3N_4 sheets and subsequently accelerate its quantum absorption capacity by exposing more active sites to irradiated light [10]. In addition, the conjugated aromatic structures within the carbon skeleton can also help to stabilized photogenerated electrons (e^-) and holes (h^+), which prolongs their lifetimes for higher ROS generation possibility [11]. Cellulose nanofiber derived carbon nanofiber (CNF) is a promising carbon candidate for g-C_3N_4 incorporation since cellulose can be easily obtained from abundant available wood biomass, and can be quickly converted to CNF with a high graphitization degree due to its inherent high carbon content [12]. Another way to enhance the photocatalytic performance of g-C_3N_4 is to employ persulfate into the system [13]. With the assistance of persulfate, more types of ROSs can be produced to boost ROP degradations.

Herein, composite photocatalysts based on cellulose carbon nanofiber incorporated g-C_3N_4 (CNF/g-C_3N_4) was prepared and used for BPA degradation under visible light with the assistance of peroxymonosulfate (PMS). The function of CNF and PMS in the reaction system and their synergistic impact on the performance of g-C_3N_4 were systematically studied. It is hypothesized that the reaction system established in this study can provide a new approach for highly efficient ROP degradation in aquatic environments.

2. Results and Discussion

2.1. Characterization of g-C_3N_4/CNF

Figure 1 shows the SEM images of cellulose nanofiber, CNF, g-C_3N_4 and CNF/g-C_3N_4. As illustrated in Figure 1a, the as-prepared cellulose nanofiber exhibited uniform filiform appearance with an average diameter of ~200–300 nm. After pyrolysis, the CNF still maintained the pristine morphology of its mother precursor with an average diameter of ~100–200 nm, except that the nanofibers were somehow curled and cracked due to the decomposition of the cellulose during high-temperature treatment (Figure 1b) [14]. Pristine g-C_3N_4 showed randomly distributed particle structure containing numerous small crystals (Figure 1c). When CNF was incorporated with g-C_3N_4, it was clearly observed from Figure 1d that two components adhered homogeneously with each other, in which the g-C_3N_4 sheets and CNF fibers were clearly revealed.

The fine morphology of CNF/g-C_3N_4 could be further investigated in terms of TEM with the results shown in Figure 2. Two components were clearly observed in Figure 2a which exhibited a uniform structure, indicating strong interactions between two components. From the magnified TEM shown in Figure 2b, it was also distinctly found that CNF integrated with g-C_3N_4, in which the nanofibers intercalated within the g-C_3N_4 sheets.

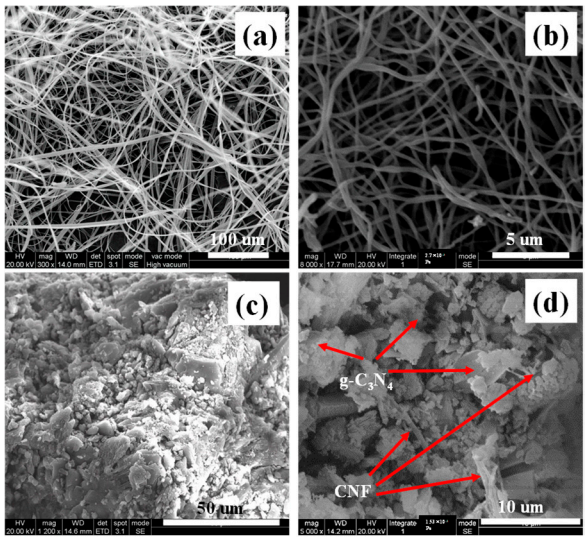

Figure 1. SEM images of (**a**) cellulose nanofiber, (**b**) CNF, (**c**) g−C_3N_4 and (**d**) CNF/g−C_3N_4.

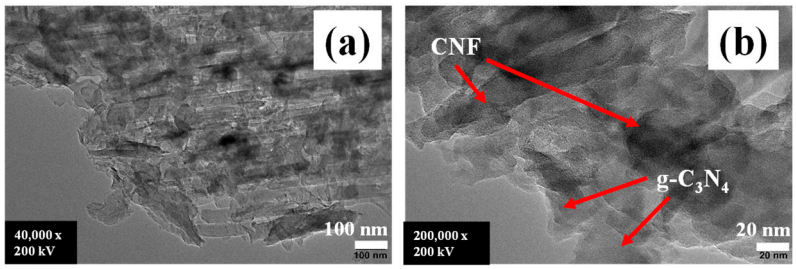

Figure 2. (**a**) TEM and (**b**) magnified TEM images of CNF/g-C_3N_4.

Figure 3a shows the XRD patterns of the prepared catalysts. As demonstrated, cellulose nanofiber contained four typical peaks located at ~12.2°, 20.1°, 22.4° and 35.6°, which were associated with the (1$\bar{1}$0), (110), (200), and (040) planes of cellulose II [15]. This meant the electrospun cellulose was regenerated cellulose instead of raw cellulose. After cellulose nanofibers were pyrolyzed, four peaks all disappeared in the pattern of the resulting CNF. Instead, two new broad peaks located at ~24° and 42° appeared, which were associated with the (002) and (100) lattice planes of a carbonaceous material [16]. This indicated that the skeleton of the carbohydrate polymer precursor was gradually converted to carbon with conjugated aromatic structures after the process was finished [17]. Figure 2a also illustrates that pristine g-C_3N_4 contained two main peaks located at ~13.4°, and 27.3°, which were indexed to the (100) and (002) planes of the hexagonal phase of g-C_3N_4 (JCPDS 87–1526) [18]. After CNF was incorporated, the CNF/g-C_3N_4 still maintained the peaks of g-C_3N_4, indicating that the incorporation of CNF did not break the structure of g-C_3N_4.

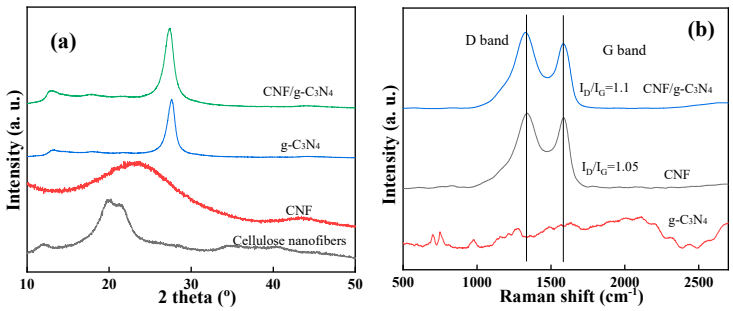

Figure 3. (**a**) XRD patterns of cellulose nanofiber, g−C_3N_4 and CNF/g−C_3N_4; (**b**) Raman spectra of CNF, g−C_3N_4 and CNF/g−C_3N_4.

The existence of CNF in CNF/g-C_3N_4 could be further investigated with Raman spectra with the results shown in Figure 3b. It was presented that the spectrum of pristine g-C_3N_4 contained many small peaks, assigning to the vibration modes of CN heterocycles. Specifically, the peaks at ~700 cm^{-1} were ascribed to the breathing modes of the s-triazine ring in g-C_3N_4. Meanwhile, the peaks located at ~1200–1300 cm^{-1} were corresponded to the lattice vibration of g-C_3N_4 crystal [19]. Furthermore, both CNF and CNF/g-C_3N_4 contained two characteristic peaks at ~1370 cm^{-1} and 1550 cm^{-1}. Generally, these two peaks represented the sp^3 bonding and sp^2 bonding in a carbonaceous material with aromatic structures, which were also named as D band and G band peaks [20]. Moreover, the intensity ratio of these two peaks (I_D/I_G) indicated the graphitization degree of the carbonaceous material [21]. As revealed in Figure 3b, the I_D/I_G value of pristine CNF was 1.05. After it was incorporated with g-C_3N_4, the I_D/I_G value of CNF/g-C_3N_4 was similar (1.10), indicating CNF was uniformly distributed within the CNF/g-C_3N_4 matrix and the graphitic structure of CNF was maintained in the composite. A high degree of the graphitic structure was helpful for accelerating the electron transfer rate during photocatlytic and PMS activation processes, thereby boosting the ROP degradation rate as a result [22].

The light response properties of the prepared photocatalysts were then studied by diffuse reflection spectrum (DRS) with the results shown in Figure 4. It was observed that pristine g-C_3N_4 had adsorption to the light from UV region to the visible region, in which the adsorption edge was located at ~440 nm. This meant that it could generate photo-energy from the visible light, which was in accordance with the previous studies [23]. After CNF was dosed with g-C_3N_4, it was clearly seen that the resulting CNF/g-C_3N_4 had a stronger response to the irradiated light, and the light adsorption edge was further extended. The involvement of CNF significantly enhanced the light absorption capability of g-C_3N_4 [24].

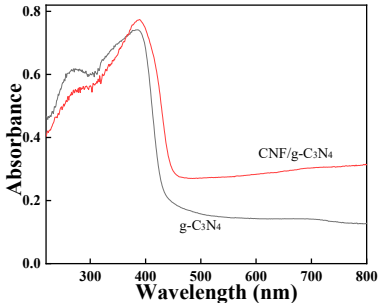

Figure 4. DRS spectra of g−C_3N_4 and CNF/g−C_3N_4.

2.2. Performance of g-C_3N_4/CNF for BPA Degradation

The catalytic activity of different systems was investigated through degrading BPA in water, with the results shown in Figure 5. The pseudo-first-order kinetic constant values (k) and their coefficients of determination (R^2) are also listed in Table 1. Since had relatively low adsorptive capability, the pre-adsorption/desorption process was omitted. Figure 5a first illustrates the performance of different prepared catalysts under the irradiation of visible light. Without the introduction of a photocatalyst, BPA was inert to irradiated light. Moreover, CNF did not show much BPA removal capability with light irradiation (k = 0.001 min^{-1}). No more than 20% of BPA was removed when the reaction time reached 120 min. Since CNF was a zero band gap conductor, the removal of BPA by CNF was mainly triggered by adsorption [25]. As a visible light photocatalyst, g-C_3N_4 was capable of degrading more than 90% of BPA within 120 min (k = 0.018 min^{-1}). When CNF was incorporated, CNF/g-C_3N_4 exhibited significantly enhanced BPA degradation capability,

in which all BPA could be removed within 90 min (k = 0.048 min^{-1}), indicating remarkable electron transfer accelerating capability of CNF.

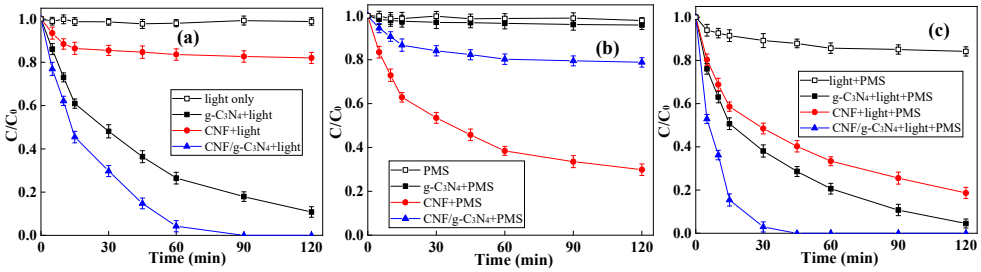

Figure 5. Catalytic performance of CNF, g-C_3N_4 and CNF/g-C_3N_4 under different reaction conditions: (**a**) visible irradiation, (**b**) PMS (2.0 mM) dosage and (**c**) visible irradiation plus PMS dosage (2.0 mM). ($[catalyst]_0$ = 0.5 g/L, $[BPA]_0$ = 0.05 mM).

Table 1. Performances of the prepared catalysts for BPA degradation.

Catalyst	Reaction System	k Value (min^{-1})	R^2
g-C_3N_4	light	0.018	0.98
	PMS	0.001	0.88
	light + PMS	0.022	0.97
CNF	light	0.001	0.96
	PMS	0.013	0.92
	Light + PMS	0.014	0.97
CNF/g-C_3N_4	light	0.048	0.97
	PMS	0.005	0.95
	Light + PMS	0.12	0.99

When light energy was changed to PMS dosing, the performances of different catalysts changed obviously. As illustrated in Figure 5b, both pure PMS and g-C_3N_4/PMS showed negligible BPA degradation activity since g-C_3N_4 did not have active sites for PMS activation on its surface. Conversely, CNF exhibited the optimal BPA degradation capability with the assistance of PMS (k = 0.013 min^{-1}). It has been reported that carbonaceous materials are capable of activating PMS with inherent oxygen containing groups [26]. Therefore, CNF was also able to activate PMS and generate ROSs for BPA degradation. Similarly, CNF/g-C_3N_4 under such circumstances could also degrade ~20% of BPA due to the existence of CNF.

When light irradiation was accompanied by PMS dosage, the BPA removal rate boosted as a result. It was first illustrated in Figure 5c that without the introduction of a catalyst, ~15% of BPA could be degraded by light plus PMS, indicating that light energy could activate a certain degree of PMS in the solution, which was in accordance with the previous studies. In addition, CNF/g-C_3N_4 was capable of degrading all BPA within 40 min under visible light irradiation with the assistance of PMS (k = 0.12 min^{-1}). Compared with the other two samples, CNF/g-C_3N_4 could integrate both high visible light absorption capability and PMS activation capability. Compared with g-C_3N_4 based photocatalyst for BPA degradation, CNF/g-C_3N_4 still exhibited remarkable BPA degradation performance (Table 2). Therefore, CNF/g-C_3N_4 was selected as the probe to investigate the mechanism in the reaction system.

Table 2. Performance comparison of g-C_3N_4 based photocatalysts for BPA degradation.

Catalyst	Light Source	Catalyst Dosage	BPA Concentration	Removal Time	Reference
CNF/g-C_3N_4+PMS	300 W Xenon lamp (CEL-PF300-T6, ZhongJiao jinyuan, Beijing, China)	0.5 g/L	0.05 mM	100%@40 min	This work
Carbon/g-C_3N_4	300 W Xenon lamp (Perfect light, Beijing, China)	0.2 g/L	0.05 mM	100%@75 min	[27]
Ag/S-g-C_3N_4	155 W Xe arc lamp (Newport 67005, Wuxi, China)	0.4 g/L	0.05 mM	80%@180 min	[28]
Fe_2O_3/g-C_3N_4+PDS	LED lamp (Yaming, Shenzhen, China)	0.5 g/L	0.05 mM	95%@60 min	[29]

The generated ROSs in the CNF/g-C_3N_4/visible light/PMS system was investigated first. Figure 6a revealed the performance of CNF/g-C_3N_4 at the existence of different classical scavengers. It was first seen that EDTA did not show inhibition on the performance of the reaction system, indicating that h^+ was not responsible for BPA degradation [22]. Under such conditions, it could be inferred that the photo-generated h^+ was quickly transferred to other ROSs. It was further illustrated from Figure 6a that TBA and MeOH provided similar impediment effects to the reaction system. Since TBA was a typical trapping agent for hydroxyl radical (·OH, k = ~6 × 10^8 $M^{-1}s^{-1}$) instead of sulfate radical (SO_4^{2-}·, k = ~4 × 10^5 $M^{-1}s^{-1}$), whereas MeOH was the trapper for both ·OH (~9 × 10^8 $M^{-1}s^{-1}$) and SO_4^{2-}· (~3 × 10^7 $M^{-1}s^{-1}$) [30], the results indicated that only ·OH participated in BPA degradation; h^+ generated under visible light and SO_4^{2-}· generated by PMS activation were both promptly changed to ·OH right after they were produced. It was also seen that L-his exhibited obvious inhibition capability towards BPA degradation, indicating the existence of singlet oxygen ($^1O_2$) in the reaction system [31]. Furthermore, the BPA degradation rate was also impeded by both Cr(VI) and p-BQ, in which the inhibition degrees by these two agents were similar. This meant the photo-generated e^- quickly reacted with dissolved oxygen in the solution and were changed to superoxide radicals ($\cdot O_2^-$) for BPA degradation [32]. Therefore, it could be verified that ·OH and $^1O_2$ were two dominant ROSs which participated in BPA degradation, and $\cdot O_2^-$ was also slightly involved in the degradation reaction.

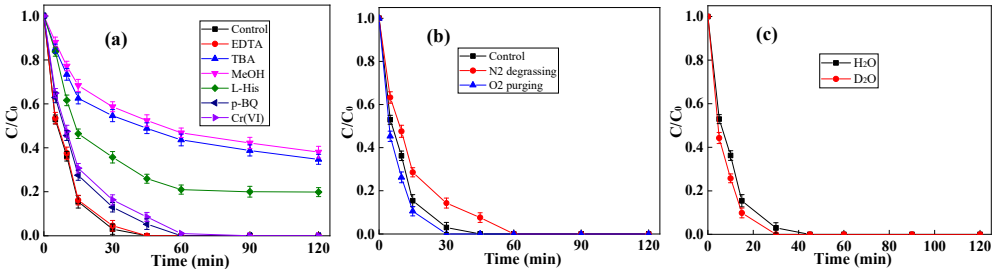

Figure 6. Performance of the CNF/g-C_3N_4/visible light/PMS system (**a**) at the existence of different scavengers, (**b**) at the existence of different gases, and (**c**) when H_2O was changed to D_2O ([catalyst]$_0$ = 0.5 g/L, [BPA]$_0$ = 0.05 mM, [PMS]$_0$ = 2.0 mM).

To confirm the deduction, the performance of the catalyst purged by different gases was then investigated, with the results shown in Figure 6b. It was seen that when the reaction solution was degassed by N_2, the BPA degradation rate slightly decreased, and the decreasing rate was similar to that at the existence of p-BQ and Cr(VI). The results implied that the e^- generated by light irradiation indeed reacted with dissolved oxygen and generated $\cdot O_2^-$ [33]. Therefore, it was further investigated in Figure 6b that when the gas was changed to oxygen, the performance of the CNF/g-C_3N_4/visible light/PMS system increased, since more $\cdot O_3^-$ could be produced for BPA degradation [34]. The existence of $^1O_2$ could be further detected by a solvent changing test. It was illustrated in Figure 6c that when H_2O was changed to D_2O, the BPA degradation rate obviously increased. Since $^1O_2$ had a longer lifetime in D_2O than H_2O [35], the results verified the generation of large amounts of $^1O_2$ which participated in BPA degradation.

The adaptability of the CNF/g-C_3N_4/visible light/PMS system was then investigated. Figure 7a shows the impact of solution pH value fluctuation on the BPA degradation rate in the reaction solution. It was clearly seen that the reaction solution could maintain its high BPA degradation activity at a wide pH range due to the existence of a variety of ROSs. The BPA degradation rate was only impeded a little when the pH value increased to 9. According to the previous studies, the pKa value of PMS was 9.4, which indicated that the activation of PMS was inhibited when the solution pH reached to 9 or higher. In addition, the BPA molecule (pKa = 9.6–10.2) was possibly deprotonated at a pH value of 9. Therefore, both BPA and PMS were not easy to attach onto the surface of CNF/g-C_3N_4 at basic condition [36]. Meanwhile, the reaction system also exhibited stable performance under the interference of different foreign inorganic ions and organic matters. It is clearly seen in Figure 7b that all BPA could be completely degraded in the reaction system within 120 min at the existence of multifarious foreign matters, indicating promising adaptability. The application potential of the CNF/g-C_3N_4/visible light/PMS system was further investigated by degrading BPA in real water matrices with results shown in Figure 7c. When deionized water was changed to tap water or lake water, 0.02 mM of BPA could still be completely degraded in the reaction system within 60 min, which implied significant implications of the reaction system for real-world water treatment.

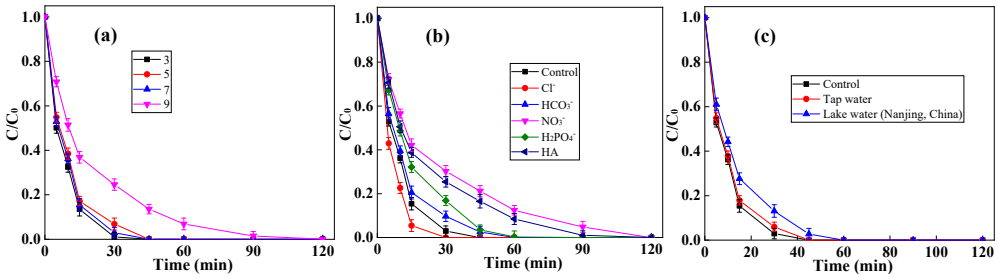

Figure 7. Impact of (**a**) pH value and (**b**) existence of foreign inorganic ions and humic acid, and (**c**) natural water matrices on the performance of the CNF/g−C_3N_4/visible light/PMS system ([catalyst]$_0$ = 0.5 g/L, [BPA]$_0$ = 0.05 mM, [PMS]$_0$ = 2.0 mM).

The long-time use stability of CNF/g-C_3N_4 was further studied by degrading BPA for consecutive cycles. Figure 8a illustrates the BPA degradation capability of the reaction system for four cycles. As revealed, all BPA could be completely degraded even at the fourth run. The performance missing might be ascribed to the gradual consumption of oxygen functional groups on CNF by continuous PMS activation [37]. Due to the existence of multiple ROSs, the reaction system also had a high TOC removal rate. Figure 8b illustrates that total organic carbon (TOC) removal rates were all higher than 60% for four runs, indicating that the CNF/g-C_3N_4/visible light/PMS system was able to mineralize BPA

without bringing about secondary pollution to the reaction solution. Furthermore, it was found from Figure 8c that recycled g-C_3N_4 still maintained its pristine structure, indicating promising long-time use stability.

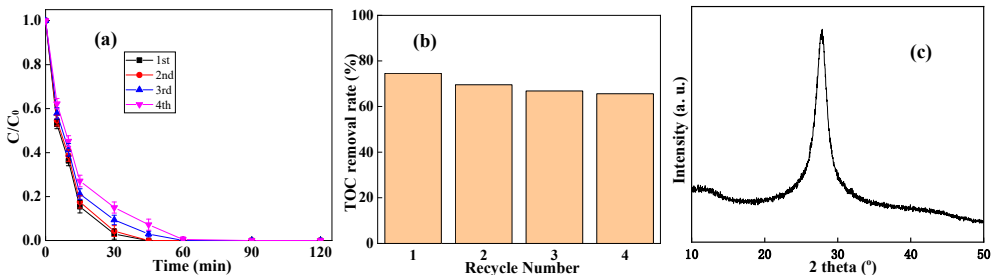

Figure 8. (**a**) Performance and (**b**) TOC removal rates of the CNF/g-C_3N_4/visible light/PMS system for four consecutive BPA degradation cycles ([catalyst]$_0$ = 0.5 g/L, [BPA]$_0$ = 0.05 mM, [PMS]$_0$ = 2.0 mM), (**c**) XRD pattern of recycled g-C_3N_4.

Based on the above results, the photocatalytic PMS activation by CNF/g-C_3N_4 for BPA degradation was proposed, which is schematically illustrated in Figure 9. When CNF/g-C_3N_4 was irradiated by visible light, the e^- at the valance band exited to the conduction band, which then either reacted with the dissolved O_2 and generated $\cdot O_2^-$, or reacted with PMS and produced $SO_4^{2-\cdot}$. $SO_4^{2-\cdot}$ was quickly transferred to ·OH by reacting with hydroxyl ion (OH^-). The h+ left on the valance band also reacted with OH^- to produce more ·OH. Simultaneously, CNF was also able to activate PMS and generate $^1O_2$. All the generated ROSs then oxidized BPA, which was finally mineralized to CO_2 and H_2O.

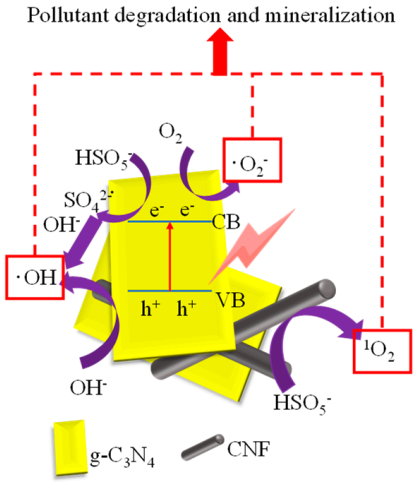

Figure 9. Schematic illustration of the BPA degradation mechanism in the CNF/g−C_3N_4/visible light/PMS system.

The impact of reaction parameters on the performance of CNF/g-C_3N_4 was finally investigated. As illustrated in Figure 10a, 0.02 mM of BPA could be promptly removed within 15 min when the dosage of the catalyst reached 0.8 g/L or higher. Even when the concentration of BPA in the solution reached as high as 0.15 mM, 0.5g/L of CNF/g-C_3N_4 could still degrade more than 90% of BPA within 120 min (Figure 10b). Both results manifested that with the assistance of PMS, CNF/g-C_3N_4 was capable of degrading BPA under visible light irradiations, which exhibited high practical application potentials.

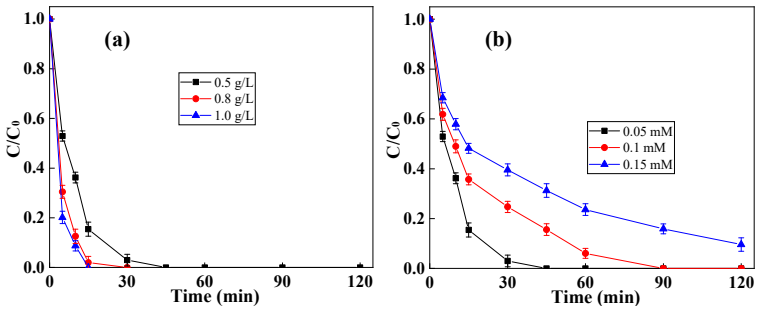

Figure 10. Impact of (**a**) catalyst dosage ($[BPA]_0$ = 0.05 mM, $[PMS]_0$ = 2.0 mM) and (**b**) BPA concentration ($[catalyst]_0$ = 0.5 g/L, $[PMS]_0$ = 2.0 mM) on the performance of the CNF/g−C_3N_4/visible light/PMS system.

3. Materials and Methods

3.1. Reagents and Chemicals

Cellulose acetate (Acetyl 39.8 wt%, hydroxyl 3.5 wt%), melamine (≥99%), Bisphenol A (BPA, ≥99%), L-histidine (L-his, 99%), humic acid (HA, AR), methanol (MeOH), t-butanol (TBA), potassium dichromate (Cr(VI), ≥99.5%) and p-benzoquinone (p-BQ, ≥99%) were purchased from Aladdin (Shanghai, China). Peroxymonosulfate $2KHSO_5{\cdot}KHSO_4{\cdot}K_2SO_4$, PMS) was purchased from Sigma Aldrich Inc. (Burlington, VT, USA). Other reagents and solvents were of analytical grade and used as received. The double distilled deionized water (H_2O) is used throughout the study.

3.2. Preparation of CNF/g-C_3N_4

The preparation of cellulose nanofibers was described in our previous study [38]. The prepared cellulose nanofiber was pyrolyzed in a tube furnace with a heating rate of 5 °C/min under N_2 atmosphere from room temperature to 800 °C, and stayed at 800 °C for 3 h. After being cooled to room temperature, CNF was obtained. The preparation of CNF/g-C_3N_4 was described as follows: based on our previous study, the yield of g-C_3N_4 produced from melamine was ~60%, and to achieve high photocatalytic performance plus high PMS activation capability [39], the incorporation amount of CNF was set at ~25 wt%. Here, 1 g melamine and 200 mg of CNF were added into 20 mL of H_2O. The solution was sonicated for 30 min and dried under magnetic stirring at 60 °C until all the H_2O was evaporated. The mixture was then transferred into a tube furnace. The tube furnace was heated to 550 °C at a heating rate of 10 °C/min under N_2 atmosphere and maintained at 550 °C for 3 h. After being cooled to room temperature, CNF/g-C_3N_4 was finally obtained. g-C_3N_4 was also prepared by pryolyzing melamine at 550 °C for 3 h following similar procedures.

3.3. Characterizations

The microstructure of the samples was observed by a scanning electron microscope (SEM, JEOL SEM 6490, Tokyo, Japan), and a transmission electron microscope (TEM, FEI F20, Hillsboro, OR, USA). An X-ray diffraction diffractometer (XRD, Rigaku Smartlab, Tokyo, Japan) was employed to analyze the crystalline structure. The graphitic structure of the samples was studied using Raman spectroscopy (Raman, Horiba Jobin Yvon HR800, Kyoto, Japan). The diffuse reflectance spectra (DRS) were conducted by a UV/Vis/NIR spectrophotometer (Perkin Elmer Lambda 950, Waltham, MA, USA). The concentration of the BPA was analyzed by high performance liquid chromatography (HPLC, Dionex Ultimate 3000, Sunnyvale, CA, USA). The total organic carbon (TOC) removal rate was determined with a TOC analyzer (Shimadzu TOC-VCPH, Tokyo, Japan).

3.4. Degradation of BPA in the CNF/g-C_3N_4/Visible Light/PMS System

If not specified, all the experiments were conducted in a 100 mL beaker with magnetic stirring containing 50 mL BPA solution with a concentration of 0.05 mM at room temperature (25 °C). A 300 W Xenon lamp (CEL-PF300-T6, ZhongJiao jinyuan, Beijing, China) with visible a light glass filter (400–700 nm, T% > 95%) at a distance 15 cm from the beaker was used as the light source. After 0.5 g/L of the catalyst and 2.0 mM of PMS was added into the BPA solution, the light was turned on. A total of 1.5 mL of the solution was taken out at pre-determined time intervals, filtered with a 0.22 μm polytetrafluoroethylene membrane and injected into 0.5 mL of fufuryl alcohol to cease the reaction. All the experiments were conducted three times, and all the data points were the average of the experiments. The photocatalytic test and PMS activation test were conducted following similar procedures in the absence of PMS or light irradiation.

4. Conclusions

To conclude, metal-free CNF/g-C_3N_4 photocatalyst was prepared in this study, which was further used for BPA degradation under visible light with the assistance of PMS. The results indicated that the incorporation of CNF significantly improved the photo-absorption capability of g-C_3N_4. Compared with g-C_3N_4, CNF/g-C_3N_4 exhibited better BPA degradation performance under visible light. When PMS was introduced into the reaction system, the CNF/g-C_3N_4/visible light/PMS system exhibited prominent BPA degradation capability, in which 0.05 mM of BPA could be completely degraded within 45 min with a high TOC removal rate (>70%). A scavenging test indicated that ·OH and $^1O_2$ were two dominant ROSs involved in BPA degradation. In addition, the reaction system also exhibited high adaptability towards various water matrices. This study demonstrates a novel way to degrade organic pollutants in water with high performance, high mineralization efficiency and high adaptability in real aquatic environments.

Author Contributions: Investigation, J.L. and G.G.; data curation, J.L. and G.G.; formal analysis, J.L.; writing—original draft preparation, J.L.; writing—review and editing, L.G.; supervision, L.G.; project administration, L.G. All authors have read and agreed to the published version of the manuscript.

Funding: This research was funded by Qinglan Project of China (2023).

Data Availability Statement: Data is available upon request.

Acknowledgments: The Advanced Analysis and Testing Center of Nanjing Forestry University is acknowledged.

Conflicts of Interest: The authors declare no conflicts of interest.

References

1. Xu, L.; Qi, L.; Han, Y.; Lu, W.; Han, J.; Qiao, W.; Mei, X.; Pan, Y.; Song, K.; Ling, C.; et al. Improvement of Fe2+/peroxymonosulfate oxidation of organic pollutants by promoting Fe2+ regeneration with visible light driven g-C3N4 photocatalysis. *Chem. Eng. J.* **2022**, *430*, 132828. [CrossRef]
2. Kim, K.-H.; Ihm, S.-K. Heterogeneous catalytic wet air oxidation of refractory organic pollutants in industrial wastewaters: A review. *J. Hazard. Mater.* **2011**, *186*, 16–34. [CrossRef]
3. Ruan, Y.; Kong, L.; Zhong, Y.; Diao, Z.; Shih, K.; Hou, L.a.; Wang, S.; Chen, D. Review on the synthesis and activity of iron-based catalyst in catalytic oxidation of refractory organic pollutants in wastewater. *J. Clean. Prod.* **2021**, *321*, 128924. [CrossRef]
4. Jin, H.; Zhu, L. Occurrence and partitioning of bisphenol analogues in water and sediment from Liaohe River Basin and Taihu Lake, China. *Water Res.* **2016**, *103*, 343–351. [CrossRef] [PubMed]
5. Lado Ribeiro, A.R.; Moreira, N.F.F.; Li Puma, G.; Silva, A.M.T. Impact of water matrix on the removal of micropollutants by advanced oxidation technologies. *Chem. Eng. J.* **2019**, *363*, 155–173. [CrossRef]

6. Wu, Y.; Fang, X.; Shen, X.; Yu, X.; Xia, C.; Xu, L.; Zhang, Y.; Gan, L. Synergetic effect of photocatalytic oxidation plus catalytic oxidation on the performance of coconut shell fiber biochar decorated α-MnO_2 under visible light towards BPA degradation. *J. Environ. Manag.* **2023**, *345*, 118911. [CrossRef] [PubMed]
7. Wen, J.; Xie, J.; Chen, X.; Li, X. A review on g-C3N4-based photocatalysts. *Appl. Surf. Sci.* **2017**, *391*, 72–123. [CrossRef]
8. Xiong, T.; Cen, W.; Zhang, Y.; Dong, F. Bridging the g-C3N4 Interlayers for Enhanced Photocatalysis. *ACS Catal.* **2016**, *6*, 2462–2472. [CrossRef]
9. Inagaki, M.; Tsumura, T.; Kinumoto, T.; Toyoda, M. Graphitic carbon nitrides (g-C3N4) with comparative discussion to carbon materials. *Carbon* **2019**, *141*, 580–607. [CrossRef]
10. Woan, K.; Pyrgiotakis, G.; Sigmund, W. Photocatalytic Carbon-Nanotube–TiO_2 Composites. *Adv. Mater.* **2009**, *21*, 2233–2239. [CrossRef]
11. Kim, J.R.; Kan, E. Heterogeneous photocatalytic degradation of sulfamethoxazole in water using a biochar-supported TiO_2 photocatalyst. *J. Environ. Manag.* **2016**, *180*, 94–101. [CrossRef] [PubMed]
12. Gan, L.; Zhong, Q.; Geng, A.; Wang, L.; Song, C.; Han, S.; Cui, J.; Xu, L. Cellulose derived carbon nanofiber: A promising biochar support to enhance the catalytic performance of $CoFe_2O_4$ in activating peroxymonosulfate for recycled dimethyl phthalate degradation. *Sci. Total Environ.* **2019**, *694*, 133705. [CrossRef] [PubMed]
13. Xu, G.; Wu, Y.; Fang, X.; Li, J.; Xu, L.; Han, S.; Cui, J.; Gan, L. One-step solvothermal synthesis of wood flour carbon fiber/BiOBr composites for photocatalytic activation of peroxymonosulfate towards sulfadiazine degradation: Mechanisms comparison between photo, chemical and photo-chemical oxidation processes. *Sep. Purif. Technol.* **2022**, *297*, 121399. [CrossRef]
14. Lédé, J. Cellulose pyrolysis kinetics: An historical review on the existence and role of intermediate active cellulose. *J. Anal. Appl. Pyrolysis* **2012**, *94*, 17–32. [CrossRef]
15. Liu, Z.; Sun, X.; Hao, M.; Huang, C.; Xue, Z.; Mu, T. Preparation and characterization of regenerated cellulose from ionic liquid using different methods. *Carbohydr. Polym.* **2015**, *117*, 99–105. [CrossRef]
16. Yu, X.; Wang, L.; Shen, X.; Wu, Y.; Xu, L.; Zhang, Y.; Shi, J.; Gan, L. New insight into the S and N co-doped poplar biochar for efficient BPA removal via peroxymonosulfate activation: S for adsorptive removal and N for catalytic removal. *Sep. Purif. Technol.* **2025**, *354*, 128809. [CrossRef]
17. Shi, J.; Dai, B.; Shen, X.; Xu, L.; Zhang, Y.; Gan, L. Wood induced preparation of Fe3C decorated biochar for peroxymonosulfate activation towards bisphenol a degradation with low ion leaching. *J. Environ. Manag.* **2023**, *340*, 117978. [CrossRef]
18. Orooji, Y.; Ghanbari, M.; Amiri, O.; Salavati-Niasari, M. Facile fabrication of silver iodide/graphitic carbon nitride nanocomposites by notable photo-catalytic performance through sunlight and antimicrobial activity. *J. Hazard. Mater.* **2020**, *389*, 122079. [CrossRef]
19. Zinin, P.V.; Ming, L.-C.; Sharma, S.K.; Khabashesku, V.N.; Liu, X.; Hong, S.; Endo, S.; Acosta, T. Ultraviolet and near-infrared Raman spectroscopy of graphitic C3N4 phase. *Chem. Phys. Lett.* **2009**, *472*, 69–73. [CrossRef]
20. Guizani, C.; Haddad, K.; Limousy, L.; Jeguirim, M. New insights on the structural evolution of biomass char upon pyrolysis as revealed by the Raman spectroscopy and elemental analysis. *Carbon* **2017**, *119*, 519–521. [CrossRef]
21. Xu, W.; Wang, L.; Shen, X.; Wu, Y.; Xu, L.; Zhang, Y.; Shi, J.; Gan, L. Lignin regulating the active sites and peroxymonosulfate activation capacities of iron incorporated 1D carbon nanofiber for efficient organic pollutant degradation. *Sep. Purif. Technol.* **2025**, *354*, 129156. [CrossRef]
22. Gan, L.; Geng, A.; Song, C.; Xu, L.; Wang, L.; Fang, X.; Han, S.; Cui, J.; Mei, C. Simultaneous removal of rhodamine B and Cr(VI) from water using cellulose carbon nanofiber incorporated with bismuth oxybromide: The effect of cellulose pyrolysis temperature on photocatalytic performance. *Environ. Res.* **2020**, *185*, 109414. [CrossRef]
23. Yang, X.; Qian, F.; Zou, G.; Li, M.; Lu, J.; Li, Y.; Bao, M. Facile fabrication of acidified g-C3N4/g-C3N4 hybrids with enhanced photocatalysis performance under visible light irradiation. *Appl. Catal. B Environ.* **2016**, *193*, 22–35. [CrossRef]
24. Tang, R.; Gong, D.; Deng, Y.; Xiong, S.; Zheng, J.; Li, L.; Zhou, Z.; Su, L.; Zhao, J. π-π stacking derived from graphene-like biochar/g-C3N4 with tunable band structure for photocatalytic antibiotics degradation via peroxymonosulfate activation. *J. Hazard. Mater.* **2022**, *423*, 126944. [CrossRef] [PubMed]
25. Cheng, N.; Wang, B.; Wu, P.; Lee, X.; Xing, Y.; Chen, M.; Gao, B. Adsorption of emerging contaminants from water and wastewater by modified biochar: A review. *Environ. Pollut.* **2021**, *273*, 116448. [CrossRef] [PubMed]
26. Wu, Q.; Zhang, Y.; Liu, H.; Liu, H.; Tao, J.; Cui, M.-H.; Zheng, Z.; Wen, D.; Zhan, X. FexN produced in pharmaceutical sludge biochar by endogenous Fe and exogenous N doping to enhance peroxymonosulfate activation for levofloxacin degradation. *Water Res.* **2022**, *224*, 119022. [CrossRef]
27. Wu, M.; He, X.; Jing, B.; Wang, T.; Wang, C.; Qin, Y.; Ao, Z.; Wang, S.; An, T. Novel carbon and defects co-modified g-C3N4 for highly efficient photocatalytic degradation of bisphenol A under visible light. *J. Hazard. Mater.* **2020**, *384*, 121323. [CrossRef]
28. Oh, W.-D.; Lok, L.-W.; Veksha, A.; Giannis, A.; Lim, T.-T. Enhanced photocatalytic degradation of bisphenol A with Ag-decorated S-doped g-C3N4 under solar irradiation: Performance and mechanistic studies. *Chem. Eng. J.* **2018**, *333*, 739–749. [CrossRef]
29. Yan, S.; Shi, Y.; Tao, Y.; Zhang, H. Enhanced persulfate-mediated photocatalytic oxidation of bisphenol A using bioelectricity and a g-C3N4/Fe2O3 heterojunction. *Chem. Eng. J.* **2019**, *359*, 933–943. [CrossRef]

30. Li, S.; Huang, J.; Li, X.; Li, L. The relation of interface electron transfer and PMS activation by the H-bonding interaction between composite metal and MCM-48 during sulfamethazine ozonation. *Chem. Eng. J.* **2020**, *398*, 125529. [CrossRef]
31. Hua, L.-C.; OuYang, R.-C.; Zhao, Z.; Nguyen, T.N.A.; Huang, C. Homogeneous versus heterogeneous Mn(II) oxidation in peroxymonosulfate assisting chlorination: Synergistic role for enhanced Mn(II) oxidation in water treatment. *Water Res.* **2024**, *265*, 122265. [CrossRef]
32. Xiao, H.; Wang, Y.; Lv, K.; Zhu, C.; Guan, X.; Xie, B.; Zou, X.; Luo, X.; Zhou, Y. N-doped biochar-Fe/Mn as a superior peroxymonosulfate activator for enhanced bisphenol a degradation. *Water Res.* **2025**, *278*, 123399. [CrossRef] [PubMed]
33. Gu, J.; Song, Y.; Yang, Y.; Guan, C.; Jiang, J. Theoretical investigation into activation of hydroperoxides by excited quinones under ultraviolet irradiation. *Chem. Eng. J.* **2023**, *463*, 142423. [CrossRef]
34. Xie, J.; Pan, X.; Jiang, C.; Zhao, L.; Gong, X.; Liu, Y. Enhanced conversion of superoxide radical to singlet oxygen in peroxymonosulfate activation by metal-organic frameworks derived heteroatoms dual-doped porous carbon catalyst. *Environ. Res.* **2023**, *236*, 116745. [CrossRef] [PubMed]
35. Lu, H.; Gan, L. Catalytic Degradation of Bisphenol A in Water by Poplar Wood Powder Waste Derived Biochar via Peroxymonosulfate Activation. *Catalysts* **2022**, *12*, 1164. [CrossRef]
36. Guan, Y.-H.; Ma, J.; Li, X.-C.; Fang, J.-Y.; Chen, L.-W. Influence of pH on the Formation of Sulfate and Hydroxyl Radicals in the UV/Peroxymonosulfate System. *Environ. Sci. Technol.* **2011**, *45*, 9308–9314. [CrossRef]
37. Ding, H.; Zhu, Y.; Wu, Y.; Zhang, J.; Deng, H.; Zheng, H.; Liu, Z.; Zhao, C. In Situ Regeneration of Phenol-Saturated Activated Carbon Fiber by an Electro-peroxymonosulfate Process. *Environ. Sci. Technol.* **2020**, *54*, 10944–10953. [CrossRef]
38. Geng, A.; Meng, L.; Han, J.; Zhong, Q.; Li, M.; Han, S.; Mei, C.; Xu, L.; Tan, L.; Gan, L. Highly efficient visible-light photocatalyst based on cellulose derived carbon nanofiber/BiOBr composites. *Cellulose* **2018**, *25*, 4133–4144. [CrossRef]
39. Han, Y.; Gan, L.; Gong, H.; Han, J.; Qiao, W.; Xu, L. Photoactivation of peroxymonosulfate by wood pulp cellulose biochar/g-C3N4 composite for diclofenac degradation: The radical and nonradical pathways. *Biochar* **2022**, *4*, 35. [CrossRef]